PHYSICAL REVIEW VOLUME 179, NUMBER 2 10 MARCH 1969

Magnon-Assisted Optical Emission in $YCrO_3$ and $LuCrO_3$

J. P. VAN DER ZIEL AND L. G. VAN UITERT
Bell Telephone Laboratories, Murray Hill, New Jersey 07974

(Received 27 August 1968)

The fluorescence spectrum of Cr^{3+} in orthorhombic $YCrO_3$ and $LuCrO_3$ was studied. Several very sharp emission lines, found at energies slightly lower than the intrinsic $^4A_2$-to-^2E absorption, are attributed to impurity-perturbed chromium ions. Magnon sideband emission, resulting in the emission of an optical photon and the simultaneous creation of a magnon at a neighboring lattice site, is observed at lower energy. Analysis of the sideband data yields values for the average nearest-neighbor exchange interaction of 22.1 and 17.6 cm^{-1} for $YCrO_3$ and $LuCrO_3$, respectively. The results are in good agreement with values of the exchange obtained from magnetic data.

I. INTRODUCTION

Magnon sidebands associated with sharp electronic optical exciton transitions in magnetically ordered materials have been under intensive experimental and theoretical study since the first observation of a sideband in MnF_2.[1] The emphasis of nearly all of the work has been on the transition-metal ion fluorides as the spin-wave spectra of most of these materials are known from inelastic neutron scattering measurements.

In this paper we discuss the emission spectrum of $YCrO_3$ and $LuCrO_3$. Values for the exchange interaction are obtained from the magnon sidebands. The spin-wave spectrum of these materials has previously not been measured. The absorption spectrum has also been observed, and will be briefly discussed.

Section II is concerned with crystal symmetry, and in Sec. III we derive an approximation to the spin-wave spectrum. The experimental results are given in Sec. IV, and are discussed in Sec. V.

The initial observation of sidebands led to the speculation that the magnon dispersion could be extracted directly from the optical-absorption data. However, more detailed investigations have shown the importance of the exciton-magnon coupling on the observed line shape, particularly when the exchange interaction of an ion in the excited state is different from the ground-state exchange.[2] Experimentally the excited-state exchange is usually found to be smaller than the ground-state exchange. The work of Dietz and Misetich[3] has shown the vibronic coupling to be an important factor in reducing the excited-state exchange. Using the Born-Oppenheimer approximation, the observed exchange interaction is the product of the true exchange and the vibronic overlap integral. Vibronic effects reduce the excited-state exchange in MnF_2; however, the insensitivity of the chromium ^2E levels to the crystal field leads us to expect that the vibronic reduction of the exchange will be relatively unimportant for the orthochromites.

The effects of exciton-magnon coupling are not present in intrinsic fluorescence or in the hot bands in absorption, since the states involved are singly occupied exciton and magnon states which are the eigenstates of the system.[3] The emission which we observe is not intrinsic, but results from ^2E-to-$^4A_2$ transitions of impurity-perturbed chromium ions.

The fluorescence from $YCrO_3$ is shown in Fig. 1. The sharp lines near 13 600 cm^{-1} are the impurity-perturbed transitions. The intrinsic $^4A_2$-to-^2E transitions observed in absorption are found near 13 700 cm^{-1}. Superimposed on a weak background we also observe strong emission near 13 400 and 13 100 cm^{-1}. As shown in Fig. 2, the emission spectrum of $YAlO_3$ with 0.1% chromium impurity is very similar to the well-known emission spectrum of Cr^{3+} in other hosts.[4] The strong 13 800-cm^{-1} line is followed by a complex of vibronic transitions involving the optical modes of the crystal.

In comparing the spectra we note the following details. First, the magnon-assisted lines at 13 400 cm^{-1} of $YCrO_3$ do not have an analog in Fig. 2. Second, the broad band at 13 100 cm^{-1} is separated by about 500 cm^{-1} from the sharp lines. Since a similar separation is found for the strong vibronic lines in Fig. 2, we tenta-

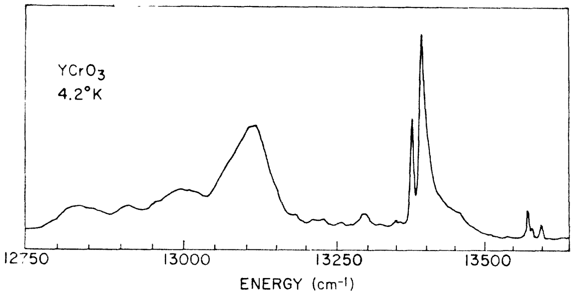

FIG. 1. Emission spectrum of $YCrO_3$.

---

[1] Magnon sideband experiments have been reviewed by D. D. Sell, J. Appl. Phys. **39**, 1030 (1968); R. Loudon, Advan. Phys. **17**, 243 (1968).

[2] R. J. Elliot, M. F. Thorpe, G. F. Imbusch, R. Loudon, and J. B. Parkinson, Phys. Rev. Letters **21**, 147 (1968); J. B. Parkinson and R. Loudon (to be published).

[3] R. E. Dietz and A. Misetich, in *Localized Excitations in Solids*, edited by R. F. Wallis (Plenum Press, Inc., New York, 1968), p. 366.

[4] D. S. McClure, in *Solid State Physics*, edited by F. Seitz and D. Turnbull (Academic Press Inc., New York, 1959), Vol. 9, p. 399.

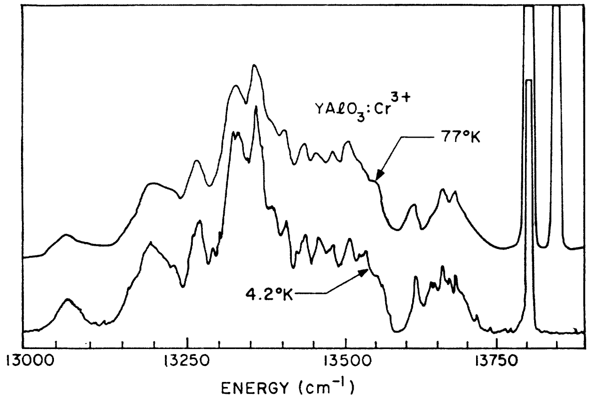

FIG. 2. Emission spectrum of $YAlO_3:Cr^{3+}$. At 4.2°K the strong line (off scale) is the transition from the lowest ^2E level to the ground state. Emission from both ^2E levels is observed at 77°K. A complex vibrational structure is observed at lower energy.

tively identify the line of Fig. 1 as a vibronic. Finally, the vibronic spectrum of $YCrO_3$ does not have the sharp structure found in the dilute crystal. This difference results from the fact that the coupling is not the same. In $YAlO_3$ the chromium ion, although an impurity, is at a center of inversion symmetry, while the emitting ions in $YCrO_3$ are perturbed by interactions with the nearby impurities, and are not at centers of inversion symmetry.

II. SYMMETRY

The structure of the orthochromites and yttrium orthoaluminate consists of four distorted perovskite units in a true crystallographic orthorhombic unit cell.[5] We shall base the unit cell on the chromium ions as shown in Fig. 3. There are four inequivalent chromium ions denoted by the letters *a–d*. The major components of spin are along the $\pm x$ axis, but an important feature of the structure is the component of the spin along the z axis which is responsible for the weak ferromagnetism.

Considerable information about the optical spectrum is obtained from symmetry considerations. The paramagnetic phase of the structure is described by the space group D_{2h}^{16}-*Pbnm*.[5] The chromium ion sites have only the inversion symmetry C_i, and electronic transitions between even-parity states are magnetic dipole. The Brillouin zone is shown in Fig. 4. Slater[6] has derived the character tables for the equivalent structure D_{2h}^{16}-*Pnma*, and the character tables of the space group *Pbnm* can be derived from Slater's tables in a straightforward manner. However, we shall be interested in the region of low temperatures where the ordering of the spins imposes additional constraints on the symmetry. For example, the antiunitary time-reversal operator K is by itself no longer a symmetry operation, and several of the spatial symmetry operations must be combined with K to take account of the spin orientation. The symmetry operations which do not include K form a unitary subgroup of the full magnetic space group, and it is this subgroup which determines the symmetry properties of the eigenstates of the magnetic crystal. The irreducible representations of the subgroup P_c2_1/m of the magnetic group $Pb'n'm$ are given in the Appendix.

As indicated in Table VII, the pure electronic transitions, namely, the $k=0$ excitons, have symmetry Γ_2^+, Γ_3^+, and Γ_4^+ in the paramagnetic group, and Γ_1^+ and Γ_2^+ in the magnetic space group. In the exciton formalism the four chromium ions are considered together, and the total spin of each sublattice has an integer value. Thus the above results are consistent with Kramer's theorem.

Compound excitations of a magnon and an exciton may occur, as shown in the Appendix, with electric dipole polarization at the points Z, R, U, and T of the Brillouin zone. We note that the selection rules for absorption are based solely on the crystal symmetry, and do not yield quantitative values for the absorption.

The sideband in impurity fluorescence has a line shape determined by both the density of magnon states and the position of the active ions relative to the impurity. Thus in this case the crystal symmetry plays a minimal role in determining the line shape.

Rao *et al.*[7] have recently found evidence of ferroelectric and pyroelectric behavior in a number of rare-

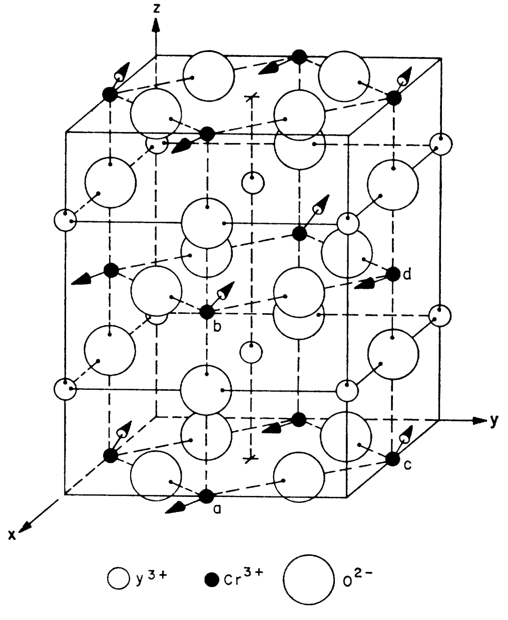

FIG. 3. Unit cell of $YCrO_3$ showing the directions of the Cr^{3+} spins at low temperature.

---

[5] S. Geller, Acta Cryst. **10**, 21 (1957).

[6] J. C. Slater, *Quantum Theory of Molecules and Solids* (McGraw-Hill Book Co., New York, 1965), Vol. 2, p. 438.

[7] G. V. Subba Rao, G. V. Chandrashekhar, and C. N. R. Rao, Solid State Commun. **6**, 177 (1968).

earth orthochromites including $YCrO_3$ and $LuCrO_3$. This observation is incompatible with the centrosymmetric space group *Pbnm.* The orthochromites may thus actually belong to a noncentrosymmetric space group. In this case the Cr^{3+} ions will not be a center of inversion and the ${}^4A_2$-to-${}^2E$ absorption can have electric dipole polarization, as, for example, is found in ruby. Yet, we observe the transitions to have purely magnetic dipole polarization. This is not inconsistent with a lack of an inversion center if the deviation is sufficiently small.

A similar situation has been observed in the ${}^4A_2$-${}^2E$ spectrum of the complex of Cr^{3+} plus a charge-compensating defect center in MgO.[8] The defect removes the inversion symmetry of the Cr^{3+} site, but the emission is found to have predominantly magnetic dipole polarization with some electric dipole character.

In the following we shall take the structure to be described by the group *Pbnm.*

III. SPIN WAVES

In this section we derive an approximation to the spin-wave spectrum.[9] In its most general form the exchange interaction between ions i and j, which is bilinear in the spins S_i and S_j, is

$$H_{ij}=+J_{ij}S_i\cdot S_j-\mathbf{D}_{ij}\cdot(S_i\times S_j)+S_i\cdot\varphi_{ij}\cdot S_j. \quad (1)$$

Here J_{ij} is the usual isotropic superexchange constant, $\mathbf{D}_{ij}$ is the antisymmetric coupling vector which gives the Dzyaloshinsky exchange, and φ_{ij} is a second-order spherical tensor of zero trace. The magnetocrystalline anisotropy energy of a ion on site i assumes the form

$$H_i{}^A=-[A^x(S_i{}^x)^2+A^z(S_i{}^z)^2+A^{xz}(S_i{}^xS_i{}^z)]. \quad (2a)$$

Applying symmetry conditions yields the anisotropy energy for an ion on the opposite sublattice

$$H_j{}^A=-[A^x(S_j{}^x)^2+A^z(S_j{}^z)^2-A^{xz}(S_j{}^xS_j{}^z)]. \quad (2b)$$

The Hamiltonian of the system then is

$$H=\sum_{i,j}H_{ij}{}^e+\sum_i H_i{}^A, \quad (3)$$

where the first sum is over distinct ion pairs and the second sum is over all the magnetic ions. It is now a straightforward, albeit somewhat tedious, procedure to obtain the spin-wave spectrum. We shall, however, make a number of approximations which greatly simplify the calculation, and yet retain a relatively accurate approximation to the spin-wave spectrum.

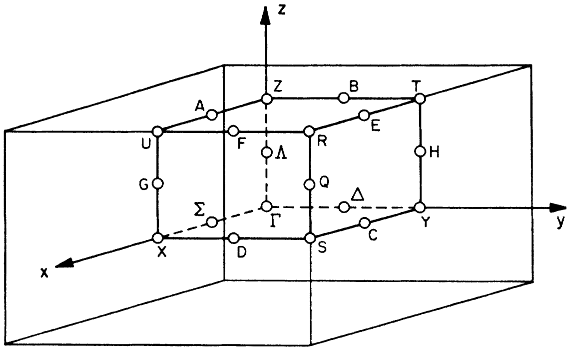

FIG. 4. Brillouin zone of the orthorhombic lattice.

The results of magnetic-moment measurements in $YCrO_3$ made by Judin and Sherman indicate that the isotropic exchange field is 35 times larger than the Dzyaloshinsky field.[10] It was further shown that the anisotropic superexchange, rather than the single-ion anisotropy, is mainly responsible for the weak ferromagnetism. Using their data, we find that the spins make an angle of less than 1° with the x axis. Furthermore, φ_{ij} is expected to be considerably smaller than D_{ij}.

We are thus justified in the following discussion to retain only the isotropic superexchange interaction. Writing the isotropic exchange coefficient between ions a and b as J_{ab}, we have from symmetry $J_{ab}=J_{dc}$ and $J_{ac}=J_{db}$. The six nearest-neighbor (nn) ions are in nearly octahedral coordination about the central ions. Using the $YCrO_3$ lattice dimensions,[11] the four nn c sites are at 3.763 Å and the two b sites at 3.766 Å with respect to the a site. Thus we expect $J_{ab}\approx J_{ac}$.

There are 12 next-nearest ions (nnn) with the same direction of spin as the central ion. These are the eight d ions at 5.354 Å and two pairs of a ions along the x and y axes at 5.241 and 5.521 Å, respectively. Using the symmetry of the crystal, we find $J_{ad}=J_{bc}$, $J_{aa}{}^x=J_{bb}{}^x=J_{cc}{}^x=J_{dd}{}^x$, and $J_{aa}{}^y=J_{bb}{}^y=J_{cc}{}^y=J_{dd}{}^y$, where $(J_{aa}{}^x)$ $(J_{aa}{}^y)$ is the exchange coefficient for ion pairs a-a along the x (y) axis.

In addition, the single-ion anisotropy A^x is included to stabilize the spins along the x axis.

We now introduce spin-wave variables in terms of local operators for which the equilibrium direction of spin is along the z axis. The transformation from the local coordinate system to the coordinate axes of the crystal is obtained by a $\frac{1}{2}\pi$ rotation about the y axis.

Labeling the spin-wave variables by the same letters as the sublattice sites of Fig. 3 and retaining bilinear

---

[8] G. F. Imbusch, A. L. Schawlow, A. D. May, and S. Sugano, Phys. Rev. **A140**, 830 (1965).

[9] L. R. Walker, in *Magnetism*, edited by G. T. Rado and H. Suhl (Academic Press Inc., New York, 1963), Vol. I, p. 299; T. Moriya, in *Magnetism*, edited by G. T. Rado and H. Suhl (Academic Press Inc., New York, 1963), Vol. I, p. 86.

[10] V. M. Judin and A. B. Sherman, Solid State Commun. 4, 661 (1966).

[11] S. Quezel-Ambrunaz and M. Marechal, Bull. Soc. Franc. Mineral. Crist. **86**, 204 (1963).

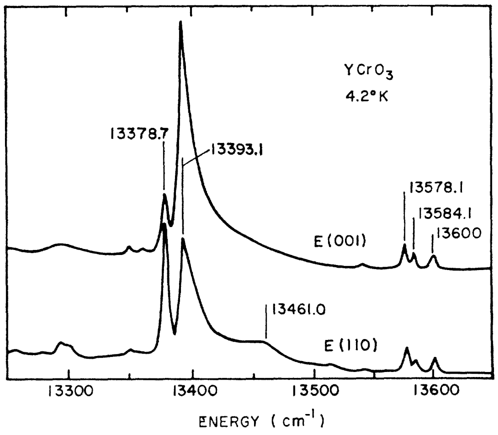

FIG. 5. Polarization of the fluorescence in the $(1\bar{1}0)$ plane.

terms gives

$$H=S\sum_k[\gamma_{ab}(0)+\gamma_{ac}(0)+\gamma_{ad}(0)$$

$$+\gamma_{aa}{}^x(0)-\gamma_{aa}{}^x(k)+\gamma_{aa}{}^y(0)-\gamma_{aa}{}^y(k)+2A^x]$$

$$\times[a_k{}^+a_k+b_k{}^+b_k+c_k{}^+c_k+d_k{}^+d_k]$$

$$+\gamma_{ab}(k)[a_k{}^+b_n{}^++a_kb_k+c_k{}^+d_k{}^++c_kd_k]$$

$$+\gamma_{ac}(k)[a_d{}^+c_k{}^++a_kc_k+b_k{}^+d_k{}^++b_kd_k]$$

$$-\gamma_{ad}(k)[a_k{}^+d_k+a_kd_k{}^++b_k{}^+c_k+b_kc_k{}^+], \quad (4)$$

where

$$\gamma_{ab}(k)=2J_{ab}\cos(\tfrac{1}{2}k_zc),$$

$$\gamma_{ac}(k)=4J_{ac}\cos(\tfrac{1}{2}k_xa)\cos(\tfrac{1}{2}k_yb),$$

$$\gamma_{ad}(k)=8J_{ad}\cos(\tfrac{1}{2}k_xa)\cos(\tfrac{1}{2}k_yb)\cos(\tfrac{1}{2}k_zc), \quad (5)$$

$$\gamma_{aa}{}^x(k)=2J_{aa}{}^x\cos(k_xa),$$

$$\gamma_{aa}{}^y(k)=2J_{aa}{}^y\cos(k_yb).$$

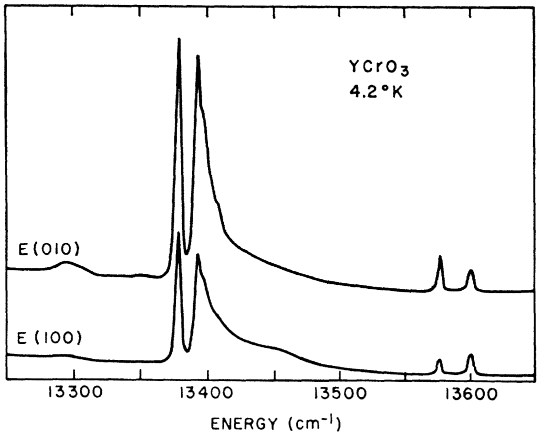

FIG. 6. Polarization of the fluorescence in the (001) plane.

To diagonalize Eq. (4) we transform to new spin-wave variables given by

$$\alpha_k=u_k(a_k+d_k)-v_k(b_k{}^++c_k{}^+), \quad (6a)$$

$$\beta_k=u_k(b_k+c_k)-v_k(a_k{}^++d_k{}^+), \quad (6b)$$

$$\gamma_k=s_k(a_k-d_k)-t_k(b_k{}^+-c_k{}^+), \quad (7a)$$

$$\delta_k=s_k(b_k-c_k)-t_k(a_k{}^+-d_k{}^+). \quad (7b)$$

The α_k and β_k are spin-wave operators for the acoustic mode, and the γ_k and δ_k are the corresponding operators for the optic mode. The u_k, v_k, s_k, and t_k are real, even functions of k and satisfy

$$u_k{}^2-v_k{}^2=2, \quad (8a)$$

$$s_k{}^2-t_k{}^2=2. \quad (8b)$$

The magnon energies of the acoustic and optic modes are

$$E_{\mathrm{ac}}=S\{[\gamma_{ab}(0)+\gamma_{ac}(0)-\gamma_{ad}(0)+\gamma_{ad}(k)-\gamma_{aa}{}^x(0)$$
$$+\gamma_{aa}{}^x(k)-\gamma_{aa}{}^y(0)+\gamma_{aa}{}^y(k)+2A^x]^2$$
$$-[\gamma_{ab}(k)+\gamma_{ac}(k)]^2\}^{1/2} \quad (9)$$

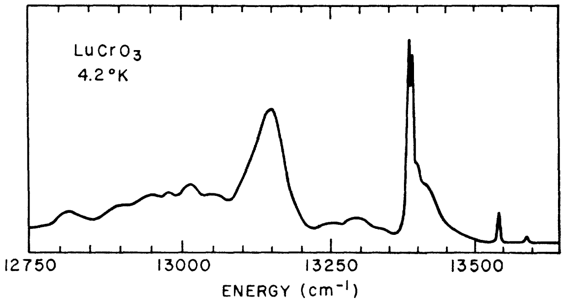

FIG. 7. Emission spectrum of LuCrO$_3$.

and

$$E_{\mathrm{opt}}=S\{[\gamma_{ab}(0)+\gamma_{ac}(0)-\gamma_{ad}(0)+\gamma_{ad}(k)-\gamma_{aa}{}^x(0)$$
$$+\gamma_{aa}{}^x(k)-\gamma_{aa}{}^y(0)+\gamma_{aa}{}^y(k)+2A^x]^2$$
$$-[\gamma_{ab}(k)-\gamma_{ac}(k)]^2\}^{1/2}. \quad (10)$$

The inclusion of the Dzyaloshinsky exchange introduces additional coupling terms in Eq. (4), which, on diagonalization, removes the degeneracy of both the acoustic and optic modes except at certain high-symmetry points on the surface of the Brillouin zone. As indicated by the magnetic measurements, these terms will be at most a few percent of the isotropic exchange constants, and will be important relative to the magnon energy only near $k\sim0$ for the acoustic mode.

IV. EXPERIMENTAL

The fluorescence data were obtained using a 1-m Czerny-Turner scanning spectrometer and a cooled S-1 response photomultiplier. Light from a 500-W Hg lamp filtered by 5 cm of saturated copper sulphate solution was used as the excitation source.

The crystals were grown from the flux by Grodkiewicz. Typically the crystals grew either as thin plates with dimensions up to $5\times5\times1$ mm^3 or as small rectangular prisms. The orientation was determined using an infrared polarizing microscope and x rays.

The polarized emission is shown in greater detail in Fig. 5. The intensities of the electronic lines near 13 580 cm^{-1} were found to be crystal-dependent. We could thus determine that the parent transition of the sidebands is the 13 578.1-cm^{-1} line. Figure 6 shows the polarization of the fluorescence in the a-b plane. Both the sharp lines and the sidebands appear in all polarizations, and thus we can not determine the dipole nature of the lines precisely. For the sidebands we note that the sum of the x and y intensities is most similar to the [110] polarization, indicating that the lines are electric dipole. A similar analysis of the 13 600-cm^{-1} lines shows that these lines may have a mixed polarization.

The emission spectrum from LuCrO$_3$, Fig. 7, is essentially the same as from YCrO$_3$. Figure 8 shows the polarization of the lines. We were again able to identify the magnon sidebands at 13 385 and 13 290.2 cm^{-1} with the parent electronic transition at 13 543.5 cm^{-1}.

The emission lifetime of several samples was measured using a repetitively pulsed light source. All the emission lines of YCrO$_3$ had a measured lifetime of 0.33 ± 0.02 msec at 4.2°K. For the LuCrO$_3$ the value was 0.26 ± 0.02 msec. Since there is no appreciable absorption at the energy of the electronic lines, the density of perturbed chromium ions is relatively low, and radiative trapping may be assumed to be negligible. Thus the lifetimes are intrinsic of the perturbed ion.

The observation of fluorescence from antiferromagnetic Cr$_2$O$_3$ has been previously reported.[12] The emission lifetimes of several crystals have now also been measured. The values for flux- and Verneuil-grown crystals are 75 and 20 μsec, respectively. The much shorter lifetime is an indication of the effectiveness of a different nonradiative mechanism in these crystals.

The absorption spectrum in the vicinity of the ^2E lines is shown in Fig. 9. Four sharp magnetic dipole lines are found near 13 700 cm^{-1}; these are the exciton-absorption lines terminating on the lowest of the split ^2E levels. The two most intense lines are polarized with H parallel to the c axis. The two magnetic dipole lines with H along the a and b axes have the same energy, but the relative oscillator strengths of the two lines are quite different.[13]

At higher energies a number of broad electric dipole lines are observed. The lines are much stronger than the magnetic dipole lines; for example, the 13 805.5-cm^{-1} line has an oscillator strength of 2×10^{-6}.

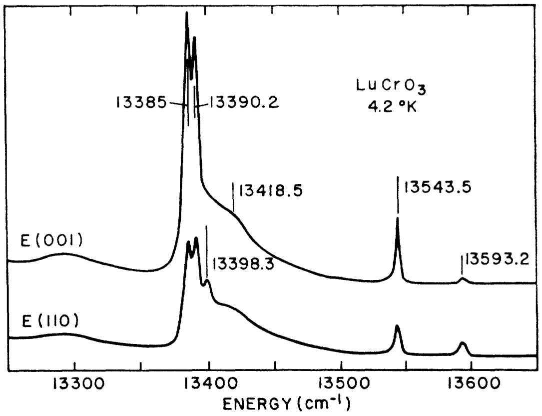

FIG. 8. Polarization of the LuCrO$_3$ fluorescence in the (1$\bar{1}$0) plane.

Measurements were made of the temperature dependence of the absorption lines. The magnetic dipole lines could be followed only up to 85°K and the electric dipole lines up to 110°K. At higher temperatures the lines broadened appreciably and could no longer be followed separately. By 85°K all the lines have shifted to lower energy by about 10 cm^{-1} from their low-temperature values. This results primarily from the change in sublattice magnetization. A much smaller shift is observed in the fluorescence of YAlO$_3$:Cr^{3+}. The electric dipole polarization and the temperature dependence indicates that the lines are either vibronics or magnon sidebands.

Finally, we note the differences between the emission and absorption spectra of Figs. 1 and 9. The emission

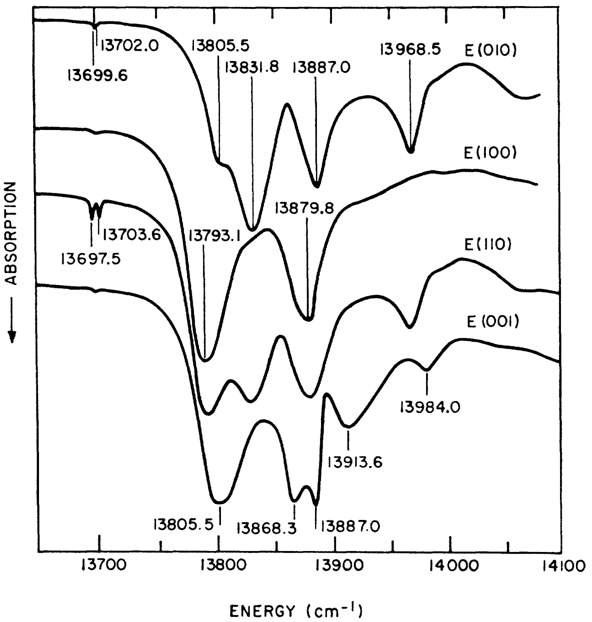

FIG. 9. Polarized absorption spectra of YCrO$_3$. The sample was 25-μ thick. The two top traces were obtained from a (001) cut plate, and the bottom traces with a (1$\bar{1}$0) plate.

---

[12] J. P. van der Ziel, Phys. Rev. **161**, 483 (1967).

[13] J. P. van der Ziel (unpublished).

sidebands do not coincide with the sidebands in absorption.

V. DISCUSSION

The sharp emission lines near 13 600 cm^{-1} originate on chromium ions perturbed by neighboring impurities and it would be of some interest to find the particular impurity which is responsible for the fluorescence. This, however, has proved not to be feasible with the flux-growth technique, since it is not possible to add quantitatively the few parts per million of impurities which are sufficient to cause the fluorescence. This is illustrated in Figs. 5 and 6, where the amplitudes of the emission lines from crystals grown in the same run from different parts of the same crucible are not the same.

The problem of impurity emission has been studied in detail for MnF_2 doped with a variety of nonmagnetic ions.[3,14,15] The emission energy is found to be determined by the type of impurity and the separation between the emitting ion and the impurity. It is the similarity of the emission characteristics of MnF_2 and $YCrO_3$ which enables us to identify the sharp emission lines of the latter as originating from perturbed chromium ions.

We shall assume, as has previously been found for MnF_2, the perturbing impurities to be nonmagnetic and located on chromium-ion sites. The impurity will then affect the energy levels of nearby chromium ions due to changes in the crystalline electric field and the exchange splitting. An estimate of the change in exchange splitting is obtained by considering, as in Sec. III, the predominant exchange interaction to be between nearest neighbors. In the molecular-field approximation, the introduction of an impurity will depress the energy levels of ions neighboring the impurity by $(3gH_{\text{ex}}-g'H_{\text{ex}}')\beta/2z$, where g and g' are the splitting factors for the ground and excited states, respectively, H_{ex} and H_{ex}' are the corresponding molecular fields, and $z=6$ is the number of nearest neighbors. Assuming $gH_{\text{ex}}\approx g'H_{\text{ex}}'$ and taking $g\beta H_{\text{ex}}\approx 200$ cm^{-1} from Fig. 5, we find the perturbed ^2E energy levels are lowered by ≈ 33 cm^{-1}. This is considerably smaller than the observed 100-cm^{-1} shift from the intrinsic lines and indicates the importance of the effects of the crystal field perturbations in reducing the $^4A_2$-^2E splitting.

A. Emission Line Shape

We now consider some specific models for sideband emission.[16] Note that in fluorescence the conservation of spin requires the magnon creation and exciton annihilation to occur on the same sublattice. The two ions involved thus must be at least second nearest neighbors. The effective electric dipole moment for the sideband is

$$P_i=\sum_{i'} P_{ii'}A_i a_{i'}^+ , \tag{11}$$

where A_i is the annihilation operator of an exciton on site i, $a_{i'}^+$ is the creation operator of a spin deviation on site i', and $P_{ii'}$ gives the coupling between i and i'.

Let us take the impurity to be at site a in Fig. 3. Excitons on nn sites to the impurity are expected to have the lowest energy, and we observe that some of nnn of such sites are also nn of the impurity. Because of the proximity to the impurity the magnon spectrum of these sites may be severely distorted. However, the sharp features of the emission near 13 400 cm^{-1} do not rule out the possibility that these are sidebands of excitons which are nn to the impurity. In MnF_2 containing Ca^{2+} one observes a sideband of the exciton which is on the first neighbor to the Ca^{2+}.[14,15] As is found experimentally, the sideband line shape is calculated to be proportional to essentially the unweighted magnon density of states. Because of differences in crystal structure the calculation of the sideband line shape of nn excitons in the orthochromites is rather difficult, and was not pursued.

In the line-shape calculations, we consider the magnon density of states to be unperturbed. This is an important assumption, and will occur when the magnon is created at a site which in the unperturbed crystal would have a small exchange interaction with the defect site. The major contributions to the sideband intensity come from **k** near the Brillouin-zone boundary, and it is mainly the short-range interactions with the nn ions which determine the energy of the peak emission intensity. The nn interactions also are the most important in determining the peaks in the magnon density of states. The two will have their maxima at the same energy if the above condition is met.

Consider next the possibility of the excitation being localized on nnn sites of the defect. We take the impurity ion to be at the origin of our coordinate system, and write the wave functions for an excitation at the $[100]$ and $[\bar{1}00]$ sites as ψ_{100} and $\psi_{\bar{1}00}$, respectively. The localized-exciton wave functions are formed from even and odd linear combinations of the single-ion excitation:

$$\psi_g=2^{-1/2}(\psi_{100}+\psi_{\bar{1}00}) , \tag{12a}$$

$$\psi_u=2^{-1/2}(\psi_{100}-\psi_{\bar{1}00}) . \tag{12b}$$

The excitation on each ion can couple to a spin deviation on the 11 occupied magnetic sites which have the same spin direction, all of which are at least nnn of the impurity. The exciton-magnon coupling along the x axis is expected to be predominant; thus we consider spin deviations of ions at $[2,0,0]$ and $[\bar{2},0,0]$. In this model the impurity, exciton, and magnon are on the

---

[14] A. Misetich, R. E. Dietz, and H. J. Guggenheim, in *Localized Excitons in Solids*, edited by R. F. Wallis (Plenum Press, Inc., New York, 1968), p. 379.

[15] R. L. Greene, D. D. Sell, R. S. Feigelson, G. F. Imbusch, and H. J. Guggenheim, Phys. Rev. **171**, 600 (1968).

[16] Similar results have been obtained for MnF_2 by A. Misetich *et al.* (Ref. 14).

same sublattice. Using the inversion symmetry of the impurity site, and the fact that the dipole moment has odd parity under inversion, we can express the effective dipole moment, Eq. (11), in terms of the even- and odd-parity exciton annihilation operators

$$A_g = 2^{-1/2}(A_{100} + A_{\bar{1}00}), \tag{13a}$$

$$A_u = 2^{-1/2}(A_{100} - A_{\bar{1}00}). \tag{13b}$$

We have

$$\mathbf{P}_g(\mathbf{k}) = -i(2/N)^{1/2}\mathbf{P}_{100,200}A_g a_k^{+} \sin(2k_x a), \tag{14a}$$

$$\mathbf{P}_u(\mathbf{k}) = (2/N)^{1/2}\mathbf{P}_{100,200}A_u a_k^{+} \cos(2k_x a). \tag{14b}$$

The transition probability for the creation of a spin wave with wave vector k is proportional to

$$(2/N)|\mathbf{P}_{100,200}|^2[|u_k|^2 + |s_k|^2], \tag{15}$$

multiplied by the joint density of exciton-magnon states. The same expression is found when the impurity ion, excitons, and spin deviations are found on the other sublattices, and also when the exciton is localized on just one of the nnn sites. Since in both cases the exciton is highly localized, its dispersion will be negligible and the line shape of the sideband thus reflects only the magnon density of states weighted by Eq. (15).

Expressions for the dipole moments involving excitons and magnons on other sites are obtained in a similar manner. For example, let the impurity and the exciton be on type-a sites as above, but consider the magnon to be created on the equivalent sites at (1,1,0). The dipole moments for this case are

$$\mathbf{P}_g(k) = -i(2/N)^{1/2}A_g a_k^{+}\{\mathbf{P}_{100,110}\sin(k_x a + k_y b) + \mathbf{P}_{100,1\bar{1}0}\sin(k_x a - k_y b)\}, \tag{16a}$$

$$\mathbf{P}_u(k) = (2/N)^{1/2}A_u a_k^{+}\{\mathbf{P}_{110,110}\cos(k_x a + k_y b) + \mathbf{P}_{100,1\bar{1}0}\cos(k_x a - k_y b)\}. \tag{16b}$$

The transition probability is proportional to the density of magnon states multiplied by

$$(2N)^{-1}[|\mathbf{P}_{100,110} + \mathbf{P}_{100,1\bar{1}0}|^2\cos^2(k_y b) + |\mathbf{P}_{100,110} - \mathbf{P}_{100,1\bar{1}0}|^2\sin^2(k_y b)][|u_k|^2 + |s_k|^2]. \tag{17}$$

Thus, in this case, the line shape is modulated by the trigonometric functions. In particular, the contributions from $|\mathbf{P}_{100,110} - \mathbf{P}_{100,1\bar{1}0}|^2$ are suppressed on the surfaces $k_y = \pm\pi/b$.

Densities of states were computed for several sets of exchange parameters. An initial calculation for nn exchange with $J_{ab} = J_{ac}$ showed that the low-energy peak of the acoustic-magnon density of states comes from contributions in the Brillouin zone where $\gamma_{ab}(\mathbf{k}) \approx 2J_{ab}$ and $\gamma_{ac}(\mathbf{k}) \approx 0$. The high-energy peak in the density of states results from the part of the zone where $\gamma_{ab}(\mathbf{k}) \approx 0$ and $\gamma_{ac}(\mathbf{k}) \approx 0$. The values of J_{ab} and J_{ac} were adjusted to give the two peaks at the proper energy. The criteria of a good fit then is that the line shapes of the experimental and theoretical curves should coincide. As shown in Fig. 10, a reasonably good fit was obtained with an unweighted acoustical-mode density of states using nn exchange values $J_{ab} = 24.8$ and $J_{ac} = 20.8$ cm^{-1} and zero anisotropy. The inclusion of the weighting factor $|u_k|^2$ tended to enhance the low-energy density of states and made the agreement with experiment somewhat worse.

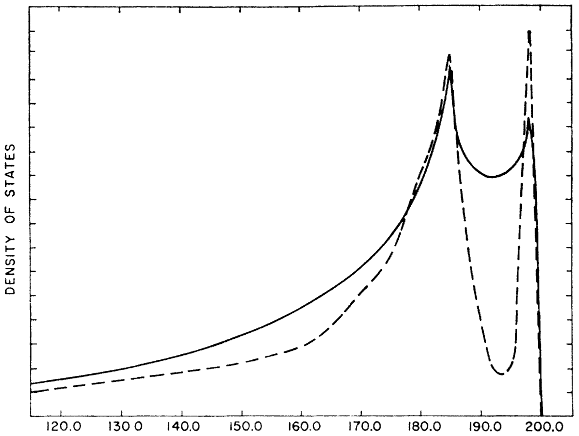

FIG. 10. Comparison of the YCrO$_3$ unweighted magnon density of states, shown by the solid curve, for the case of nn interactions, with the line shape observed in [010] polarization (dashed curve).

The acoustic and optic modes are degenerate on the surface of the Brillouin zone, and the maximum density of states of the optic mode is coincident with the high-energy peak of the acoustic mode. As shown by the above examples, Eqs. (15) and (17), both modes are weighted equally by trigonometric functions and the two peaks cannot be separately attributed to the acoustic and optic modes. Inclusion of the optic mode gave a much larger peak at 199.4 cm^{-1} than was actually observed.

The line shape particularly between the two peaks could not be reproduced more accurately than Fig. 10 even with the inclusion of nnn exchange. This would appear to result from unknown weighting factors in the transition probability rather than in drastic differences in the density of states.

For LuCrO$_3$ the values for nn exchange were $J_{ab} = 13.4$ and $J_{ac} = 19.7$. The separation between the sideband peaks is much smaller than for YCrO$_3$. The smallness of the dip between the peaks in the emission results primarily from the width of the no-magnon line and the finite spectrometer resolution relative to the peak separation.

A better fit to the data might be achieved if the spin-wave spectrum were known. However, the agreement

TABLE I. Experimental and theoretical values of $\bar{J}$ (in cm^{-1}).

	$YCrO_3$	$LuCrO_3$
Present experiment	22.1	17.6
Molecular field, T_N	13.1	10.4
Molecular field, θ	23.3	18.5
BPW	16.5	13.1
Series expansion	19.4	15.3

is about as good as is obtained from the sidebands of impurity emission in MnF_2. Clearly a more detailed knowledge of the defects and the sites on which the excitons or magnons are created would also give additional insight in the line shape and polarization of the spectra.

B. Comparison with Theory

It is of some interest to compare the values of the exchange obtained here with the more classical results of magnetic theory. The results of such an analysis are shown in Table I and are discussed below.

The first row gives the average exchange integral

$$\bar{J}=\sum_j z_j J_{ij}/\sum_j z_j\,, \tag{18}$$

obtained using the data from Sec. V A. Here z_j is the number of type-j neighbors of ion i with exchange integral J_{ij}.

The next row gives results of the molecular-field (MF) approximation.[17,18] The relation (in cm^{-1}) between the exchange and Néel temperature T_N is

$$\bar{J}=3T_N/zS(S+1)\,. \tag{19}$$

The values of T_N are 140.6 and 112.4°K, respectively, for $YCrO_3$ and $LuCrO_3$.[19] The MF approximation is notorious for giving low values of J. This is because a more exact approximation relates the paramagnetic Curie-Weiss temperature θ to the exchange by

$$\theta=-S(S+1)\tfrac{1}{3}\sum_j z_j J_{ij}\,, \tag{20}$$

and $-\theta/T_N$ ranges from 1.1 to 1.5 for the simple antiferromagnets. Unfortunately, accurate measurements of θ are not available for the materials studied here; however, the ratio has an experimental value of 1.78 for the very similar material $LaCrO_3$.[17,20] This result was obtained from measurements of χ^{-1} in the range $2T_N<T<3T_N$. If the measurements had been carried out to still higher temperature, perhaps a somewhat smaller value might have been found. The use of this ratio gives the value of exchange obtained from Eq. (20) shown in the third row. The difference with the experimental values is about 5%.

The fourth row gives the results of the Bethe-Peierls-Weiss (BPW) calculation relating the exchange integral to the Néel temperature. The relations derived by Smart were used in this calculation and also for the MF approximation.[17] A factor of -2 has been introduced to relate Smart's exchange Hamiltonian to Eq. (1). The BPW method again underestimates the value of the exchange interaction.

A more accurate relation between the exchange and T_N is obtained by expanding the inverse susceptibility above T_N in a power series of T_N/T.[21,22] For a cubic antiferromagnet, Rushbrooke and Wood have found

$$T_N=(5\bar{J}/192)(z-1)[11S(S+1)-1]\times[1-0.63/zS(S+1)]\,. \tag{21}$$

For $S=\frac{3}{2}$ this reduces to

$$\bar{J}=0.197T_N\,. \tag{22}$$

The exchange constants are given in the last row of Table I, and are about 13% smaller than the experimental values.

These results indicate that the series-expansion method gives the most accurate results in relating $\bar{J}$ to T_N; however, the "exact" relation between $\bar{J}$ and θ is found to be considerably more accurate.

ACKNOWLEDGMENTS

We are grateful to R. E. Dietz, M. Eibschütz, L. M. Holmes, D. D. Sell, and M. D. Sturge for helpful discussions, and to Miss B. B. Cetlin for computer assistance. The technical assistance of F. L. Clark in the course of the experimental work is appreciated.

APPENDIX: SPACE GROUPS *Pbnm* AND P_c2_1/m

The primitive translations of the orthorhombic lattice are $\mathbf{t}_1=a\hat{x}$, $\mathbf{t}_2=b\hat{y}$, and $\mathbf{t}_3=c\hat{z}$, where $\hat{x}$, $\hat{y}$, and $\hat{z}$

TABLE II. Character table for the point $\Gamma(0,0,0)$ of the group *Pbnm*.

	$\Gamma_1^{\pm}$	$\Gamma_2^{\pm}$	$\Gamma_3^{\pm}$	$\Gamma_4^{\pm}$
$\{E\|0\}$	1	1	1	1
$\{C_{2z}\|\tau\}$	1	-1	1	-1
$\{C_{2y}\|\tau_2\}$	1	1	-1	-1
$\{C_{2x}\|\tau_1\}$	1	-1	-1	1
$\{I\|0\}$	±1	±1	±1	±1
$\{\sigma_z\|\tau\}$	±1	∓1	±1	∓1
$\{\sigma_y\|\tau_2\}$	±1	±1	∓1	∓1
$\{\sigma_x\|\tau_1\}$	±1	∓1	∓1	±1

---

[17] J. S. Smart, J. Phys. Chem. Solids **11**, 97 (1959).

[18] J. S. Smart, in *Magnetism*, edited by G. T. Rado and H. Suhl (Academic Press Inc., New York, 1963), Vol. III, p. 63.

[19] R. Aleonard, J. Marechal, R. Pauthenet, J. P. Rebouillat, and V. Zarubica, Compt. Rend. **262**, 799 (1966).

[20] G. H. Jonker, Physica **22**, 707 (1956).

[21] G. S. Rushbrooke and P. J. Wood, Mol. Phys. **6**, 409 (1963).

[22] M. Eibschütz, S. Shtrikman, and D. Treves, Phys. Rev. **156**, 562 (1967).

TABLE III. Character table for the points $\Gamma(0,0,0)$, $X(\pi/a,0,0)$, $Y(0,\pi/b,0)$, and $S(\pi/a,\pi/b,0)$ of the group P_c2_1/m. The notation of the representations at the points X, Y, and S is identical with the Γ notation.

	$\Gamma_1^{\pm}$	$\Gamma_2^{\pm}$
$\{E\|0\}$	1	1
$\{C_{2z}\|\tau\}$	1	-1
$\{I\|0\}$	±1	±1
$\{\sigma_z\|\tau\}$	±1	∓1

are unit vectors in the x, y, and z directions, respectively. The nonprimitive translations of the group *Pbnm* are $\boldsymbol{\tau}=\frac{1}{2}c\hat{z}$, $\boldsymbol{\tau}_1=\frac{1}{2}(a\hat{x}+b\hat{y})$, and $\boldsymbol{\tau}_2=\frac{1}{2}(a\hat{x}+b\hat{y}+c\hat{z})$. The vectors of the reciprocal lattice are $b_1=2\pi/a$, $b_2=2\pi/b$, and $b_3=2\pi/c$. The characters of the irreducible representations of the point Γ of *Pbnm* are given in Table II.[23] Here $\{E|0\}$ is the identity operator, $\{C_{2z}|\boldsymbol{\tau}\}$ is a twofold rotation about the z axis followed by a translation $\boldsymbol{\tau}$, $\{I|0\}$ is the inversion operator, $\{\sigma_z|\boldsymbol{\tau}\}=\{C_{2z}|\boldsymbol{\tau}\}\{I|0\}$, and the meaning of the remaining symmetry operations is obtained by a permutation of the coordinate axes. The complete set of symmetry operations of the group consists of the product of the operations in Table II and the subgroup of primitive translations $\{E|\mathbf{t}\}$.

TABLE IV. Character table for the points $Z(0,0,\pi/c)$, $R(\pi/a,\pi/b,\pi/c)$, $U(\pi/a,0,\pi/c)$, and $T(0,\pi/b,\pi/c)$ of the group P_c2_1/m. There is one twofold degenerate representation for each of the points.

	Z_1
$\{E\|0\}$	2
$\{C_{2z}\|\tau\}$	0
$\{I\|0\}$	0
$\{\sigma_z\|\tau\}$	0

TABLE V. Character table for the points $\Sigma(\alpha,0,0)$, $\Delta(0,\beta,0)$, $A(\alpha,0,\pi/c)$, $B(0,\beta,\pi/c)$, $C(\alpha,\pi/b,0)$, $D(\pi/a,\beta,0,)$, $E(\alpha,\pi/b,\pi/c)$, and $F(\pi/a,\beta,\pi/c)$ of the group P_c2_1/m. The notation for the representations at the points Δ, A, B, C, D, E, and F is identical with the Γ notation.

	Σ_1	Σ_2
$\{E\|0\}$	1	1
$\{\sigma_z\|\tau\}$	1	-1

The orientation of the spins in the magnetic phase is shown in Fig. 3. The structure is described by the magnetic space group $Pb'n'm$, were the primes denote that the time-reversal operator is associated with the spatial symmetry operation. Thus the operations of the magnetic group are $\{E|0\}$, $\{C_{2z}|\boldsymbol{\tau}\}$, $\{I|0\}$, $\{\sigma_z|\boldsymbol{\tau}\}$, $\{C_{2x}K|\boldsymbol{\tau}_1\}$, $\{C_{2y}K|\boldsymbol{\tau}_2\}$, $\{\sigma_xK|\boldsymbol{\tau}_1\}$, and $\{\sigma_yK|\boldsymbol{\tau}_2\}$.

TABLE VI. Character table for the points $\Lambda(0,0,\gamma)$, $Q(\pi/a,\pi/b,\gamma)$, $G(\pi/a,0,\gamma)$, and $H(0,\pi/b,\gamma)$ of the group P_c2_1/m. The notation of the representations at the points Q, G, and H is identical with the Λ notation. $\omega=\exp(i\gamma c)$.

	Λ_1	Λ_2
$\{E\|0\}$	1	1
$\{C_{2z}\|\tau\}$	ω	$-\omega$

The space subgroup containing only the unitary operations is P_c2_1/m. The base-centered P_c unit cell is defined by chromium ions of types a and c of Fig. 3. The character tables of the irreducible representations of the unitary subgroup, shown in Tables III–VI were obtained using Döring's algebraic method.[24] The symmetry properties of the magnetic and electric dipole moments are given in Table VII.

TABLE VII. Selection rules for radiative processes for the space groups *Pbnm* and P_c2_1/m.

	S_x	S_y	S_z	x	y	z
Pbnm	Γ_4^+	Γ_2^+	Γ_3^+	Γ_4^-	Γ_2^-	Γ_3^-
P_c2_1/m	Γ_2^+	Γ_2^+	Γ_1^+	Γ_2^-	Γ_2^-	Γ_1^-

The symmetry of the compound exciton-magnon states can now be found using the product of the characters method of Lax and Hopfield.[25] It can be shown that the decomposition of the products at the Z, R, U, and T points of the Brillouin zone results in an electric dipole moment having components in the x, y, and z direction. No electric dipole moment is found for the products at the points X, Y, or S.

---

[23] G. F. Koster, J. O. Dimmock, R. G. Wheeler, and H. Statz, *Properties of the Thirty-two Point Groups* (McGraw-Hill Book Co., New York, 1962).

[24] W. Döring, Z. Naturforsch. **14A**, 343 (1959).

[25] M. Lax and J. J. Hopfield, Phys. Rev. **124**, 115 (1964).